Research
Antimicrobial Resistance—Article

A Rigid Nanoplatform for Precise and Responsive Treatment of Intracellular Multidrug-Resistant Bacteria

Shaoqi Qu [a], Xiaoyong Huang [a], Xiangbin Song [a], Yifan Wu [a], Xiaowei Ma [a], Jianzhong Shen [a,b], Kui Zhu [a,b,*]

[a] National Center for Veterinary Drug Safety Evaluation, College of Veterinary Medicine, China Agricultural University, Beijing 100193, China
[b] Guangdong Laboratory for Lingnan Modern Agriculture, Guangzhou 510642, China

ARTICLE INFO

ABSTRACT

Antibiotic treatment failure against life-threatening bacterial pathogens is typically caused by the rapid emergence and dissemination of antibiotic resistance. The current lack of antibiotic discovery and development urgently calls for new strategies to combat multidrug-resistant (MDR) bacteria, especially those that survive in host cells. Functional nanoparticles are promising intracellular drug delivery systems whose advantages include their high biocompatibility and tunable surface modifications. Inspired by the fact that the rigidity of nanoparticles potentiates their cellular uptake, rigidity-functionalized nanoparticles (RFNs) coated with bacteria-responsive phospholipids were fabricated to boost endocytosis, resulting in the increased accumulation of intracellular antibiotics. Precise delivery and high antibacterial efficacy were demonstrated by the clearing of 99% of MDR bacteria in 4 h using methicillin-resistant *Staphylococcus aureus* (MRSA) and pathogenic *Bacillus cereus* as models. In addition, the subcellular distribution of the RFNs was modulated by altering the phospholipid composition on the surface, thereby adjusting the electrostatic effects and reprograming the intracellular behavior of the RFNs by causing them to accurately target lysosomes. Finally, the RFNs showed high efficacy against MRSA-associated infections in animal models of wound healing and bacteremia. These findings provide a controllable rigidity-regulated delivery platform with responsive properties for precisely reprograming the accumulation of cytosolic antibiotics, shedding light on precision antimicrobial therapeutics against intracellular bacterial pathogens in the future.

1. Introduction

Antibiotic resistance is regarded as a global major public health crisis [1]. For example, *Staphylococcus aureus* (*S. aureus*)—especially methicillin-resistant *S. aureus* (MRSA)—causes volatile chronic and recurrent infections, leading to severe disease and high mortality in both humans and animals [2]. Furthermore, bacteria have evolved multiple strategies to survive under antibiotic stresses, such as antibiotic tolerance [3,4]. Antibiotic tolerance can facilitate the eventual rapid development of antibiotic resistance *in vivo* [3]. Alarmingly, antibiotic tolerance mediated by hosts is universal and has been largely underestimated for diverse species of classic extracellular bacteria [5–7]. For example, *S. aureus* can persist and replicate in either macrophages or epithelial cells to tolerate high levels of antibiotics due to the latter's poor cellular penetration. Intracellular pathogens such as Trojan horses exacerbate the antibiotic resistance crisis [8]. In addition, the discovery and devel-

opment of new antibiotics have slowed and almost stopped, as almost no new classes of antibiotics have been approved by the US Food and Drug Administration (FDA) since the late 1980s [9,10]. Therefore, alternative intervention strategies are urgently required to address cytosolic bacterial infections by restoring the efficacy of existing antibiotics.

Nanoparticles are promising and effective delivery systems for accumulating intracellular drugs through surface modification or the adjustment of particle size [11,12]. Mesoporous silica nanoparticles (MSNs) with high surface area, good biocompatibility, and biodegradability have attracted intensive attention as carriers for drug delivery [13]; however, the mechanical properties of MSNs have largely been neglected. Meanwhile, the cellular uptake of drugs mediated by intrinsically rigid nanoparticles such as MSNs remains unclear [14]. Very recently, it has been shown that nanoparticle rigidity plays a crucial role in compartmentalizing and concentrating drugs into distinct subcellular compartments [15]. Thus, rigidity-regulated delivery systems represent alternative strategies to target persistent bacteria in host cells. Moreover, drug delivery systems that are triggered to release drugs hold

* Corresponding author.
E-mail address: zhuk@cau.edu.cn (K. Zhu).

considerable promise for improving the treatment of infections by minimizing selective pressure and enhancing drug efficacy [16]. For example, great advances have been made using nanogels, self-assembled nanoparticles, and biomimetic materials through the recognition of endogenous stimuli for drug release [17–19]. Therefore, the combination of precision therapy and rigidity-regulated cellular uptake will shed light on the future design of tunable antibiotic delivery platforms to combat multidrug-resistant (MDR) bacterial pathogens.

Herein, we designed facile and biocompatible phospholipid-coated silica nanoparticles to facilitate rigidity-regulated cellular uptake and subcellular delivery of encapsulated antibacterial agents. MSNs serve as the skeleton of these rigidity-functionalized nanoparticle (RFN) delivery systems. MSNs were covered with phospholipids to form a responsive outer membrane, and the resulting RFNs were further loaded with antibiotics (Fig. 1). RFNs can boost rigidity-mediated endocytosis and the on-demand release of antibiotics to precisely kill bacterial pathogens of interest. Furthermore, subcellular redistribution of antibiotics can be achieved by tuning the phospholipid composition of RFNs to potentiate antibacterial efficacy. Our findings show that RFNs can be easily equipped with the capabilities of precise recognition, rigidity-enhanced endocytosis, and subcellular compartmentalization; thus, they provide a promising nanoplatform against intracellular bacterial infections.

2. Materials and methods

2.1. Materials

Tetraethyl orthosilicate (TEOS) and triethanolamine (TEA) were obtained from Aladdin (China). Phospholipase A$_2$ (PLA$_2$, P9279) and phospholipase C (PLC, P6621) were obtained from Sigma-Aldrich (USA). Distearoyl phosphatidylglycerol (PG), dimyristoyl phosphatidylcholine (PC), and cholesterol were purchased from AVT Pharmaceutical Technology Co., Ltd. (China). The fluorescent lipophilic dyes 3,3′-dioctadecyloxacarbocyanine perchlorate (Dio) and 1,1′-dioctadecyl-3,3,3′,3′-tetramethylindocarbocyanine perchlorate (Dil) were purchased from Beyotime (China). Rifampin (RIF) was obtained from the China Institute of Veterinary Drug Control (China). Deionized water was produced using a Milli-Q Plus water filtration system (USA).

2.2. Preparation of rigidity-functionalized nanoparticles

PG, PC, and cholesterol were dissolved in chloroform and mixed at a mass ratio of 8:2:1. A solution containing a total of 1 mg of phospholipids was evaporated to dryness at room temperature overnight. Then, the resulting film was hydrated and extruded with 5 mg of MSNs. Extrusion was performed using two polycarbonate membranes (Whatman, USA) with 200 nm pore sizes and repeated 22 times. RFNs were purified by centrifugation in a Microcon-30 kDa centrifugal filter unit (EMD Millipore, USA) at 4000g for 15 min. Dio- and Dil-labeled RFNs were prepared using the same method.

2.3. Drug loading

RIF was loaded into the MSNs via a wetness impregnation method [19]. In brief, RIF was dissolved in methanol at a concentration of 5 mg·mL^{-1} and incubated with MSNs at a concentration of 10 mg·mL^{-1} for 30 min. RIF-loaded MSNs were obtained by centrifugation at 10 000g for another 15 min at 4 °C. The supernatants were collected to test the concentration of unloaded RIF using
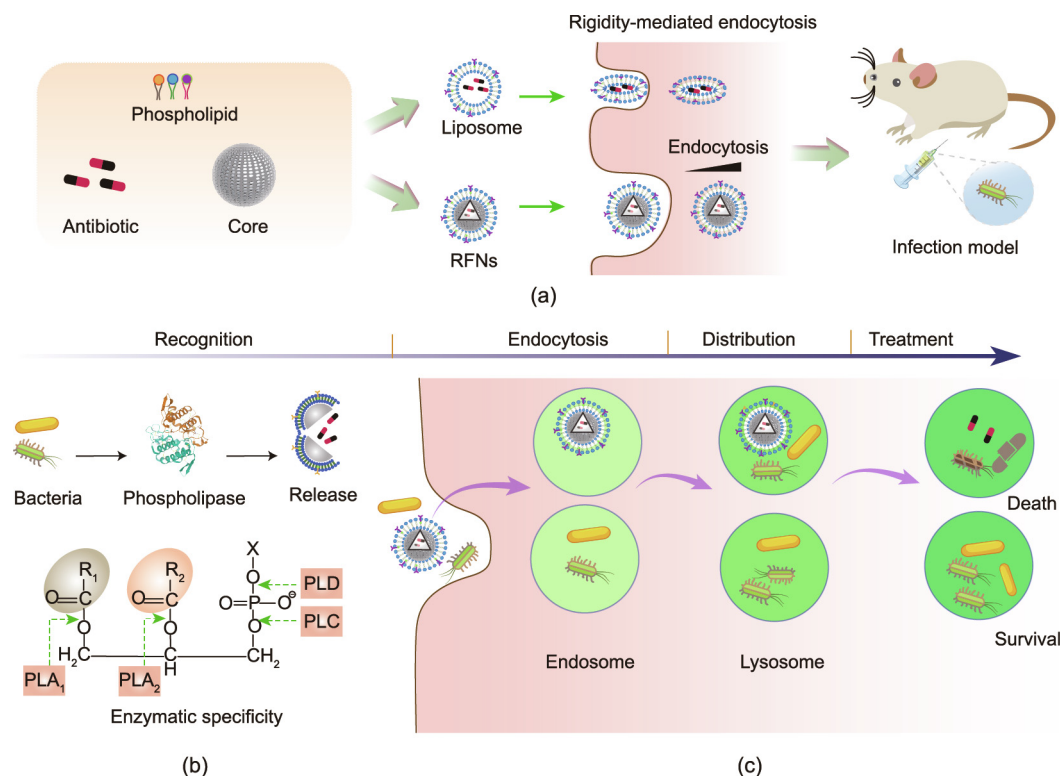

Fig. 1. Schematic illustration of RFNs targeting bacteria in lysosomes via endocytosis for precision therapy. (a) The rigidity of the functional nanoparticles was used to enhance their cellular uptake for precision therapy. Antibiotics were encapsulated within MSNs coated with phospholipids and subsequently applied to enhance cytosolic delivery, leading to improved efficiency against cytosolic bacteria. (b) Schematic diagram of phospholipase-degradable RFNs with specific recognition. The incorporation of enzyme-sensitive phospholipids into the RFNs allows antibiotics to be rapidly released at the infection site in response to the phospholipase secreted by MDR bacteria. Sites of action of various phospholipases are presented. (c) Subsequent internalization of RFNs by the endocytic pathway, which leads to the eradication of cytosolic bacteria. PLA1 and PLA2: phospholipase A1 and A2; PLC and PLD: phospholipase C and D.

spectrophotometry. MSNs loaded with RIF without a phospholipid coating are denoted as NPs.

2.4. In vitro drug release

NPs and RFNs containing 500 μg of RIF were incubated at 37 °C in 1 mL of phosphate-buffered saline (PBS). The particles were then centrifuged in a Microcon-10 kDa centrifugal filter unit (EMD Millipore) by centrifugation (4000g, 4 °C for 15 min). To investigate PLC-triggered drug release, PLC at a final concentration of 1 unit·mL^{-1} was incubated with each sample. Tricyclodecan-9-yl-xanthogenate (D609; final concentration 1 μmol·L^{-1}), a specific PLC inhibitor, was used to inhibit PLC enzymatic activity. The concentration of released RIF was quantified by measuring the absorbance of the supernatants with a multifunctional microplate reader (Infinite M Plex, Tecan, Switzerland) at 474 nm. Nanoparticles were maintained in the incubator at each time point (0.5, 1, 2, 4, 8, 12, 16, and 24 h) for drug release.

2.5. Killing kinetics

Bacillus cereus (B. cereus) MHI241 was cultured overnight in brain heart infusion (BHI; Land Bridge Technology, China) at 37 °C with shaking at 200 r·min^{-1} to reach the exponential growth phase. The concentration of the microbial solution was adjusted to the initial McFarland 0.5 solution. The solution was then further diluted ten-fold. Bacterial populations were challenged with RIF (1.25 μg·mL^{-1}), NPs (40 μg·mL^{-1}), or RFNs (160 μg·mL^{-1}) at a concentration corresponding to ten-fold the minimum inhibitory concentration (MIC). After incubation at 37 °C with shaking (200 r·min^{-1}), the bacterial samples were removed from each well at predetermined time points (0, 2, 4, 8, and 24 h) for a series of ten-fold dilutions. The diluted bacterial suspensions (100 μL) were spread onto trypticase soy agar plates (TSA; Land Bridge Technology, China) and incubated at 37 °C for 16–20 h. Colonies were counted and the colony-forming units (CFUs) per milliliter (CFUs·mL^{-1}) were calculated.

2.6. Cells and cell culture

Human hepatocellular carcinoma (HepG2), mouse macrophage cells (RAW 264.7), and lung carcinoma cells (A549) were maintained in a modified medium (Dulbecco's modified Eagle's medium (DMEM); Gibco, USA) containing 10% heat-inactivated fetal bovine serum (FBS; Invitrogen, USA) and 1% (w/v) penicillin–streptomycin (Sigma-Aldrich, USA) at 37 °C in a humidified atmosphere of 5% CO$_2$.

2.7. Intercellular distribution

The distribution of Dil-labeled RFNs was observed by seeding 5×10^5 cells on top of 14 mm round coverslips in a 24-well plate, growing to 70%–80% confluence, and treating the cells with NPs or RFNs (50 μg·mL^{-1}) at 37 °C in 5% CO$_2$ for 1 h. After incubation, the cells were washed with PBS three times to remove any particles that were not taken up. Cells were fixed in 4% paraformaldehyde for 10 min, washed with PBS for 5 min, and stained with 4′,6-diamidino-2-phenylindole (DAPI) and Actin Green 488 reagent (a high-affinity F-actin probe). The coverslips were mounted on glass slides with an anti-quenching agent, dried, and kept in the dark until examination with a Leica TCS SP8 confocal laser scanning microscope (CLSM; Wetzlar, Germany).

RAW 264.7 cells were treated with RFNs (50 μg·mL^{-1}) and fluorescently labeled B. cereus (multiplicity of infection (MOI) = 40) and incubated at 37 °C in 5% CO$_2$ for 2 h. After incubation, the cells were washed with PBS (pH 7.4) three times to remove any particles and bacteria that were not taken up. The cells were stained with LysoTracker Deep Red (50 nmol·L^{-1}, Invitrogen). The samples were kept in the dark until examined by CLSM.

2.8. PG-regulated cellular uptake

RFNs with different components of phospholipids (percentage of PG: 0, 20%, 40%, 60%, 80%, and 100%) were prepared to modulate cellular uptake. Particle-treated RAW 264.7 cells were incubated at 37 °C in 5% CO$_2$ for 1 h. After incubation, the cells were washed with PBS three times to remove any particles that were not taken up. Cells were fixed in 4% paraformaldehyde for 10 min and then washed with PBS three times. The cells were stained with DAPI (Beyotime) and Actin Green 488 reagents (Life Technologies, USA) and observed by means of CLSM.

2.9. Pathway of cellular uptake

RAW 264.7 cells were co-treated with RFNs (50 μg·mL^{-1}) and fluorescently labeled B. cereus (MOI = 40), followed by incubation at 37 °C in 5% CO$_2$ for 0.5 and 1 h, respectively. After incubation, the cells were washed with PBS (pH 7.4) three times to remove any particles and bacteria that were not taken up. The early and late endosomes in the cells were detected by means of immunofluorescence. The primary antibodies included rabbit anti-Rab7 and mouse anti-EEA1 antibodies (Abcam, UK), and the secondary antibodies were goat anti-rabbit and goat anti-mouse antibodies (Beyotime). The samples were prepared and kept in the dark until examined by CLSM.

2.10. In vitro antibacterial tests

RAW 264.7 cells were infected with B. cereus stained with pHrodo Red (Life Technologies) at 37 °C for 15 min at an MOI of 40 and cultured with ten-fold the MIC of RIF, NPs, or RFNs at 37 °C in 5% CO$_2$ for 4 h. After a 100 μg·mL^{-1} gentamicin treatment and washing with PBS (pH 7.4) three times, the cells were fixed with 4% paraformaldehyde at room temperature for 10 min and permeabilized with 0.1% Triton X-100 in PBS (pH 7.4) for 10 min. Samples were stained with DAPI and Actin Green 488 for fluorescence determination by CLSM.

RAW 264.7 cells were infected with B. cereus at an MOI of 40 and then treated with ten-fold the MIC of RIF, NPs, or RFNs for 4 h. Gentamicin (100 μg·mL^{-1}) was used to kill the extracellular bacteria. After washing three times with PBS, the cells were lysed with 1% Triton X-100 for 2 min. The diluted cell lysates (100 μL) were spread onto TSA plates and incubated at 37 °C for 16–20 h. The colonies were counted, and the CFUs per milliliter were calculated.

2.11. Ethics statement

All animal procedures were performed in accordance with the guidelines for the Administration of Affairs Concerning Experimental Animals approved by the State Council of the People's Republic of China (Date issued: 11–14-1988). The protocols and details were approved by the Institutional Animal Care and Use Committee (IACUC) of the China Agricultural University (Approval No. AW50301202-2–1). Male Wistar rats (five weeks old) and female BALB/c mice (18–20 g) were housed with controlled 12-h light/12-h dark cycles and had free access to sterile food and water. The environment was maintained under specified pathogen-free conditions at a constant temperature ((23 ± 2) °C) and humidity (60% ± 5%).

2.12. Rat skin wound infection model

To evaluate the therapeutic effects of RFNs against a clinical isolate of MRSA T144, a rat skin wound infection model was used. Rats were anesthetized by intraperitoneal (*i.p.*) chloral hydrate (0.5 mL, 10%, w/w) and disinfected by swabbing with alcohol (75%, v/v) before the operation. The fur on the back of each rat was carefully removed, and a full-thickness wound with a diameter of 1 cm was generated. The rats were infected with MRSA T144 (1×10^8 CFUs per wound) suspended in 50 µL of PBS (pH 7.4). All animals were divided into four groups: PBS (pH 7.4), vancomycin (Van; 5 mg·kg^{-1} body weight), NPs (equivalent to 2 mg·kg^{-1} RIF), and RFNs (equivalent to 2 mg·kg^{-1} RIF). The size and bacterial loads of the wounds were tested at various time points (0, 3, 6, 9, and 13 d) following the treatments. Wound tissues were collected and stored at –20 °C until they were homogenized in 1 mL of sterile PBS. For CFU analysis, the obtained homogenates were plated on *S. aureus* chromogenic agar medium (CHRO Magar, France) after ten-fold serial dilutions and incubated at 37 °C for 16–20 h. In addition, the body weights and complete healing times of all animals were recorded. Serum was collected from the rats on day 3 and stored at –80 °C until analysis of the concentrations of tumor necrosis factor-α (TNF-α) and interleukins 1β (IL-1β) using enzyme-linked immunosorbent assay (ELISA) kits (Beyotime) according to the manufacturer's instructions. On day 13, the wounds were excised and fixed in a 4% paraformaldehyde fix solution (Beyotime). All tissues were then embedded in paraffin, and 4 µm sections were prepared for traditional hematoxylin and eosin (H&E) and Masson staining.

2.13. Mouse bacteremia model

Female BALB/c mice were randomly divided into four groups: PBS (pH 7.4), Van (5 mg·kg^{-1} body weight), NPs (equivalent to 2 mg·kg^{-1} RIF), and RFNs (equivalent to 2 mg·kg^{-1} RIF). MRSA T144 (7.5×10^7 CFUs) suspended in 100 µL of PBS was intravenously administered through the tail vein. Therapy was administered to the appropriate mice at 1 h post-infection via intravenous injection. The mice were monitored for two days. Once a mouse died, its heart, liver, spleen, lungs, and kidneys were immediately collected and stored at –20 °C until analysis. The surviving mice were euthanized by cervical dislocation to collect different organs after 48 h. Organ homogenates were prepared in 1 mL of sterile PBS and serially diluted, plated on *S. aureus* chromogenic agar medium, and incubated at 37 °C for 16–20 h. Bacterial loads (Log_{10}CFU of MRSA T144) in the different organs were determined. The survival rates of all groups were calculated after two days.

2.14. Statistics

Statistical significance was determined using the software package GraphPad Prism 7.0. All data are presented as means ± standard deviation (SD). All calculations of *P* values were performed using an unpaired *t*-test or one-way analysis of variance (ANOVA) and other special analyses.

3. Results

3.1. RFNs exhibit high selectivity and efficacy in combating bacterial pathogens

RFNs with biodegradable phospholipids as caps were fabricated via functionalized surface modification of MSNs to actively recognize phospholipase-positive bacteria, leading to antibiotic release in an on-demand manner to precisely kill the targeted bacteria

(Fig. 2(a)). MSNs with high dispersity and a uniform spherical morphology were obtained by using cetyl trimethyl ammonium bromide (CTAB) as the porogen to induce a mesoporous structure [20], based on scanning electron microscopy (SEM) and dynamic light scattering (DLS) analyses (Figs. 2(b) and (c)). MSNs with small pore sizes were further observed by transmission electron microscopy (TEM; Fig. 2(b)), and quantified by the nitrogen (N$_2$) absorption–desorption technique (3.8 nm, Figs. 2(c) and (d)). The density functional theory (DFT) surface area and pore volume of the MSNs were 490.2 m^2·g^{-1} and 0.92 cm^3·g^{-1} (Fig. 2(e)), respectively, indicating the formation of mesopores. Meanwhile, the concentration of CTAB was optimized to obtain MSNs with an appropriate size (130 nm) and the highest RIF loading capacity (9.7% ± 0.9%; Fig. S1 in Appendix A). Furthermore, we analyzed the CTAB residue (67.1 ng·mg^{-1}) in the RFNs by liquid chromatography-tandem mass spectrometry (Fig. S2 in Appendix A), which was appropriate for the subsequent studies.

To coat phospholipids onto the surface of MSNs by means of noncovalent linkages, we used the hydration/extrusion method [18]. MSNs were coated with PG and PC to form phospholipase-reactive RFNs for controlled release. PG and PC were mixed at a mass ratio of 8:2 to prevent leakage and maintain biocompatibility during blood circulation. We observed a noticeable core–shell structure based on TEM analysis (Fig. 2(b) and Fig. S3 in Appendix A), suggesting successful phospholipid translocation to the surface of the MSNs. Moreover, the particle size of the MSNs increased after the phospholipid bilayer coating process, indicting phospholipid encapsulation (Fig. S4 in Appendix A). Successful loading of RIF into the RFNs was observed at 474 nm (Fig. 2(f)) and confirmed by the characteristic absorptions using Fourier-transform infrared spectroscopy (Fig. S5 in Appendix A). We further observed a stable hydrodynamic diameter and surface zeta potential of the RFNs after treatment at –80 °C for as long as 30 d (Fig. S6 in Appendix A).

We hypothesized that phospholipid hydrolysis catalyzed by bacteria-derived phospholipase could cause exposure of the pore structure in RFNs, to release the loaded antibiotics. To evaluate the feasibility of the use of phospholipase-responsive RFNs for antibacterial activity, we first assessed the responsiveness of the RFNs using PLC from *B. cereus* and PLA$_2$ from *S. aureus* for *in vitro* release tests. Compared with only 20% RIF liberated in the medium after incubation for 24 h, more than 60% RIF was released from the RFNs in the presence of PLC (Fig. 2(g)). The PLC-responsive release was diminished in the presence of a specific PLC inhibitor (1 µmol·L^{-1}, D609, Fig. 2(g)). The sustained release of RIF from the RFNs enhanced the therapeutic efficacy by prolonging the release duration. The different drug release kinetics also suggested that the RFN pore structure was covered by the phospholipid coating, which was consistent with the core–shell structure observed by TEM (Fig. 2(b)). Furthermore, we observed that the RFNs eradicated 99.9% of *B. cereus* after incubation for 8 h (Fig. 2(g) and Fig. S7 in Appendix A) and exhibited robust antibacterial activity against MRSA (Fig. S8 in Appendix A). The coating was disrupted by phospholipases, which accelerated the release of RIF from the RFNs. Collectively, these results suggest that RFNs are highly responsive to phospholipase-positive bacteria and can serve as a potent platform to increase the selectivity of antibiotics.

3.2. RFNs target lysosomes by tuning the phospholipid composition

Antibiotics with poor ability to enter cells have greatly limited efficacy against cytosolic bacteria [21]. Distribution of intracellular antibiotics in mammalian cells plays a critical role in ablating cytosolic bacteria [5]. We next explored the intracellular pathways and targets of RFNs in cells. The chemical composition and surface properties of nanoparticles are crucial in their uptake, intracellular distribution, and therapeutic efficacy [22,23]. Therefore, we
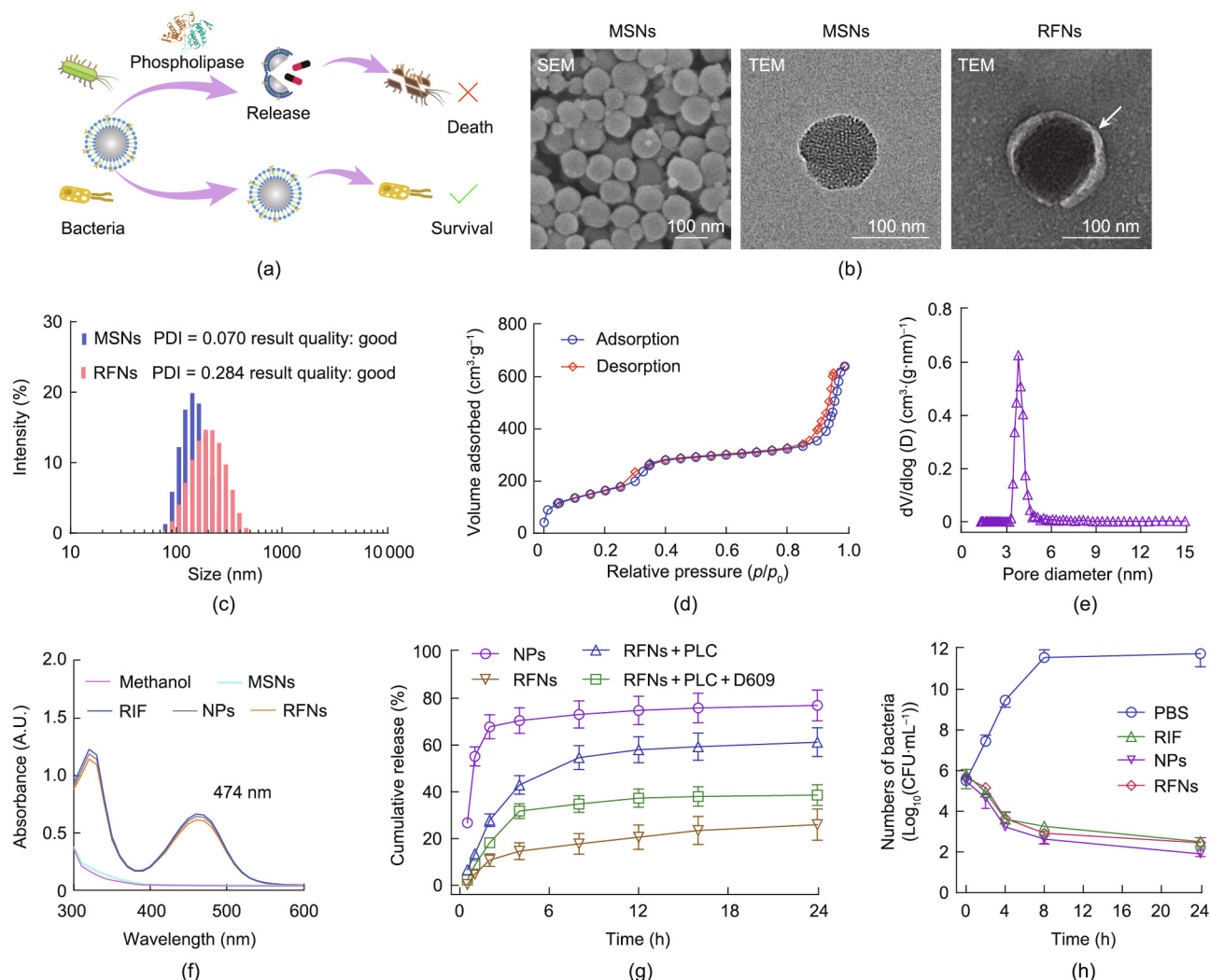
Fig. 2. RFNs efficiently kill phospholipase-secreting bacteria with high selectivity. (a) Schematic illustration of the high selectivity of RFNs against MDR bacteria. (b) Representative images of MSNs and RFNs coated with phospholipase-sensitive phospholipids. The arrow indicates the phospholipid coating. Scale bar: 100 nm. (c) The increase in the size of RFNs after coating with phospholipids was determined using DLS. (d) Nitrogen adsorption–desorption isotherms and (e) the corresponding pore-size distribution of MSNs. (f) Absorption spectra of RIF under different conditions with a maximum at a wavelength of 474 nm. (g) Release of RIF from the RFNs initiated by PLC in PBS for 24 h. The release of RIF was inhibited by D609, which is a specific inhibitor of PLC. (h) Time-kill kinetics of *B. cereus* at the exponential growth phase treated with ten-fold the MIC of RIF, NPs, and RFNs. All data are presented as the means ± SD. PDI: polydispersity; dV/dlog (D): pore volume against pore diameter; p/p_0=tested pressure/saturated pressure.

deciphered the phospholipid compositions on the RFNs and their intracellular distribution in RAW 264.7 cells. The PG/PC content on the RFN surface sharply affected the RFNs' intracellular distribution (Fig. 3(a) and Fig. S9 in Appendix A). RFNs with 80% PC were broadly distributed within the cells, suggesting that high PC content in the coating leads to nanoparticles escaping from lysosomes into the cytosol. In contrast, punctate distribution was located in the intracellular region in the presence of RFNs with 20% PC, indicating that RFNs may be trapped in lysosomes. Notably, a similar trend was observed in lung carcinoma cells A549 (Fig. S10 in Appendix A). Moreover, the increase of lysosomal accumulation of RFNs was dose-dependent on the PG/PC content (Fig. 3(b)). Positively charged phospholipids and human-derived phospholipids decreased the lysosomal accumulation of RFNs (Fig. S11 in Appendix A), which was consistent with previous studies reporting that positive charges triggered endosomal membrane destabilization [24]. Nevertheless, it was unclear whether the phase-transition temperature of the phospholipids participated in their regulation of distribution [25]. Altogether, these findings suggested that the subcellular distribution of RFNs could be precisely modulated by

changing their phospholipid components, and that a high PG/PC ratio facilitates the lysosomal targeting process.

Given that many intracellular bacteria are eventually trapped in lysosomes [6], it is critical to promote antibiotic accumulation in lysosomes in order to eradicate cytosolic bacterial pathogens. We found colocalization of the RFNs with bacteria and lysosomes, which suggested that RFNs and bacteria localize in the same subcellular compartment (Fig. 3(c)). Consequently, the phospholipase derived from bacteria efficiently hydrolyzed the coating on the RFNs to activate the release of antibiotics and precisely target cytosolic bacteria [25,26]. Furthermore, we observed extensive binding of RFNs (green) to *B. cereus* (blue) (Fig. 3(c)), based on the electrostatic interaction between PC and the predominant teichoic acid in the cell wall of *B. cereus* [27]. RFNs with high PG/PC ratios can not only target lysosomes but also trap bacteria in the subcellular compartment. Therefore, we further determined the cellular uptake pathway of the RFNs. To visualize the cytosolic localization of RFNs during *B. cereus* infection, RAW 264.7 cells infected with *B. cereus* were stained with endosomal markers. The RFNs and *B. cereus* colocalized with early endosomes and late endosomes
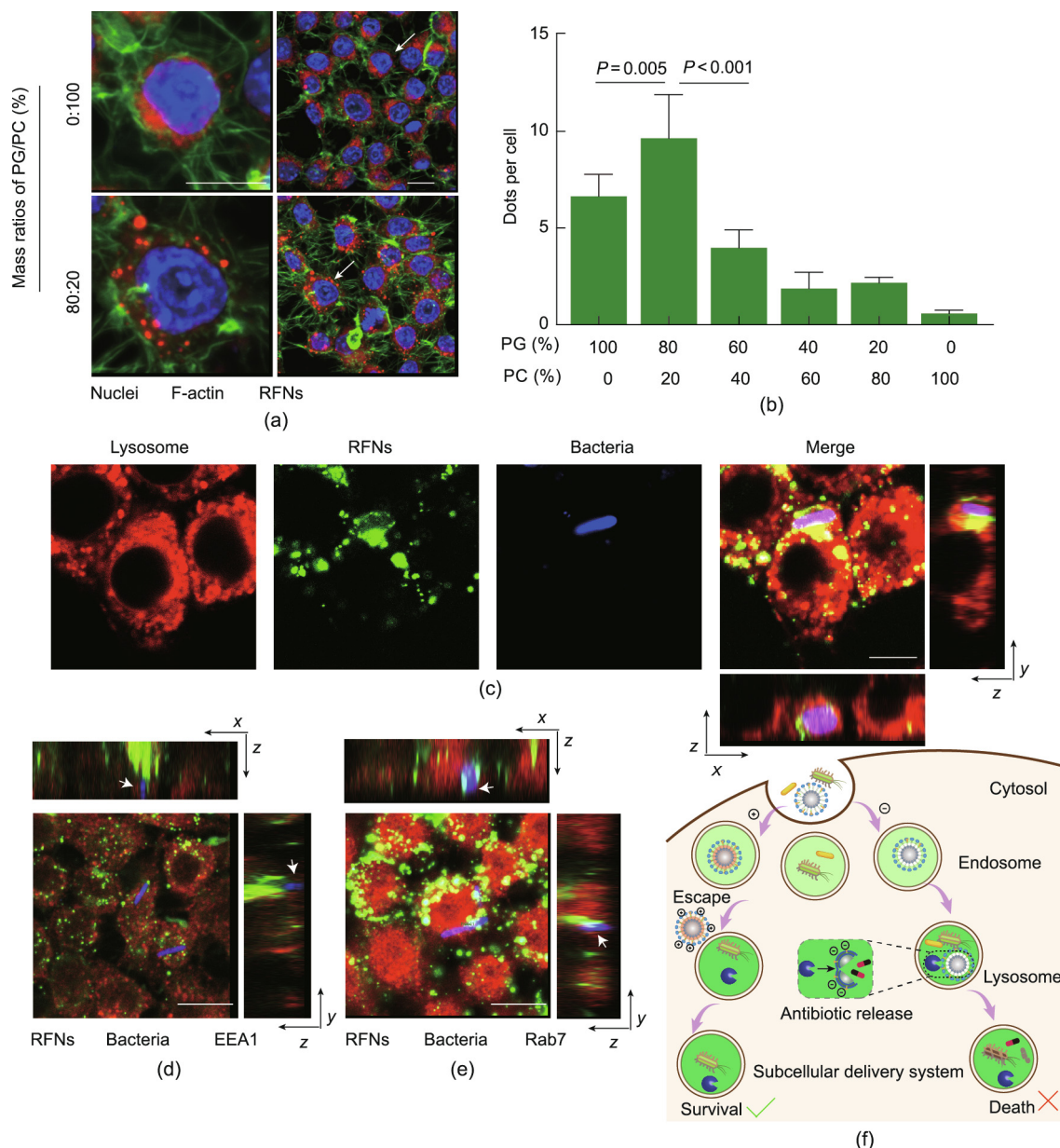
Fig. 3. Cellular uptake of RFNs modulated by varying PG/PC contents. (a) Increased ratios of PG/PC in the phospholipid coating mediate the punctate distribution of RFNs in RAW 264.7 cells. Representative confocal images are provided of RAW 264.7 cells incubated with RFNs composed of various PG compositions (80% and 20%) for 1 h. The cells were stained with DAPI (blue) and Actin Green 488 (green). Scale bar: 10 μm. (b) An increase in dots per cell was observed in RAW 264.7 cells treated with RFNs with increased PG/PC contents. Statistical significance was determined by nonparametric one-way ANOVA. (c) Representative images of RAW 264.7 cells treated with RFNs (50 μg·mL^{-1}) and *B. cereus* MHI241 (MOI = 40) for 2 h. Lysosomes (red) colocalized with the bacteria (blue) and RFNs (green). Scale bar: 8 μm. (d, e) RAW 264.7 cells were treated with (d) RFNs (50 μg·mL^{-1}) and (e) *B. cereus* MHI241 (MOI = 40) for 0.5 and 1 h. Cells were stained with antibodies against EEA1 (early endosomes) and Rab7 (late endosomes). Scale bar: 10 μm. (f) RFNs work against cytosolic bacteria by targeting subcellular compartments.

after 1 h of treatment (Figs. 3(d) and (e)); this finding suggested that RFNs and bacteria may enter the cell via endocytosis, which is consistent with the internalization of the majority of polymer nanoparticles [28]. Similar results were also obtained in the *S. aureus* model, indicating the potent feasibility and versatility of the RFNs (Fig. S12 in Appendix A). Collectively, these results indicated that we successfully fabricated a controllable delivery platform with antibiotic redistribution to target cytosolic bacterial pathogens (Fig. 3(f)).

3.3. RFNs exhibit high antibacterial efficacy in vitro

Incomplete clearance of bacterial pathogens inside host cells can allow these infected cells to act as Trojan horses, leading to relapse and the recurrence of infections [29]. Given the attractive targeting ability of RFNs to deliver antibiotics into host cells, we further investigated the antibacterial efficiency of RFNs against cytosolic *B. cereus* and *S. aureus*. Our results showed that RFNs effectively reduced the loads of cytosolic *B. cereus* in infected RAW 264.7 cells (Fig. 4(a) and Fig. S13 in Appendix A). The numbers of *B. cereus* in the presence of RFNs were approximately 100-fold lower than those in cells treated with RIF alone for 4 h (Fig. 4(b)). This powerful ability of RFNs to remove cytosolic bacteria was also confirmed in the *S. aureus* model (Fig. S14 in Appendix A), which can be attributed to the precisely targeted delivery. In this way, the RFNs demonstrated their potential against cytosolic bacterial infection in a subcellular targeting manner.

Given the attractive ability of RFNs to eliminate cytosolic bacteria, we tested the biochemical changes in *B. cereus* treated with RFNs. We observed a dose-dependent increase in membrane permeability (Fig. S15(a) in Appendix A) and the release of cellular macromolecules such as β-galactosidase (M_w = 130 kDa, Fig. S15(b) in Appendix A)) and adenosine triphosphate (ATP; Fig. S15(c) in Appendix A) from *B. cereus* treated with RFNs. Further analysis of membrane depolarization revealed increased dissipation of the *B. cereus* membrane potential in a dose-dependent manner after RFN treatment (Fig. 4(c)). Depolarization of the membrane potential impairs many important biochemical reactions that occur on the membrane, including the generation of ATP in bacteria [6]. Consequently, we assayed the accumulation of intracellular ATP. As expected, RFN treatment led to decreased intracellular ATP in *B. cereus* (Fig. 4(d)). In addition, the accumulation of endogenous reactive oxygen species (ROS) is crucial for bacterial clearance [30]. We observed an increase in ROS accumulation in *B. cereus*

with increasing RFN concentrations (Fig. 4(e)). Taken together, these results indicate that membrane injury and oxidative damage are essential for RFN antimicrobial activity.

3.4. RFNs protect animals against MRSA infection

To determine the capabilities of RFNs against bacterial infection *in vivo*, we investigated their therapeutic potential in two *in vivo* models using MRSA T144 cells (Fig. 5(a)). Cell viability (Fig. S16 in Appendix A) and hemolysis rate (Fig. S17 in Appendix A) with RFNs were performed before the pharmacodynamic evaluation. RFNs showed good biocompatibility even at a concentration of 500 μg·mL^{-1}, which is an unachievable dose *in vivo*. Rat skin wounds were infected with MRSA T144 (1×10^8 CFUs per wound), and treatments were performed at the wounded sites 1 h after infection, according to our previously reported method [22,31]. We found that the infected wounds treated with RFNs (equivalent
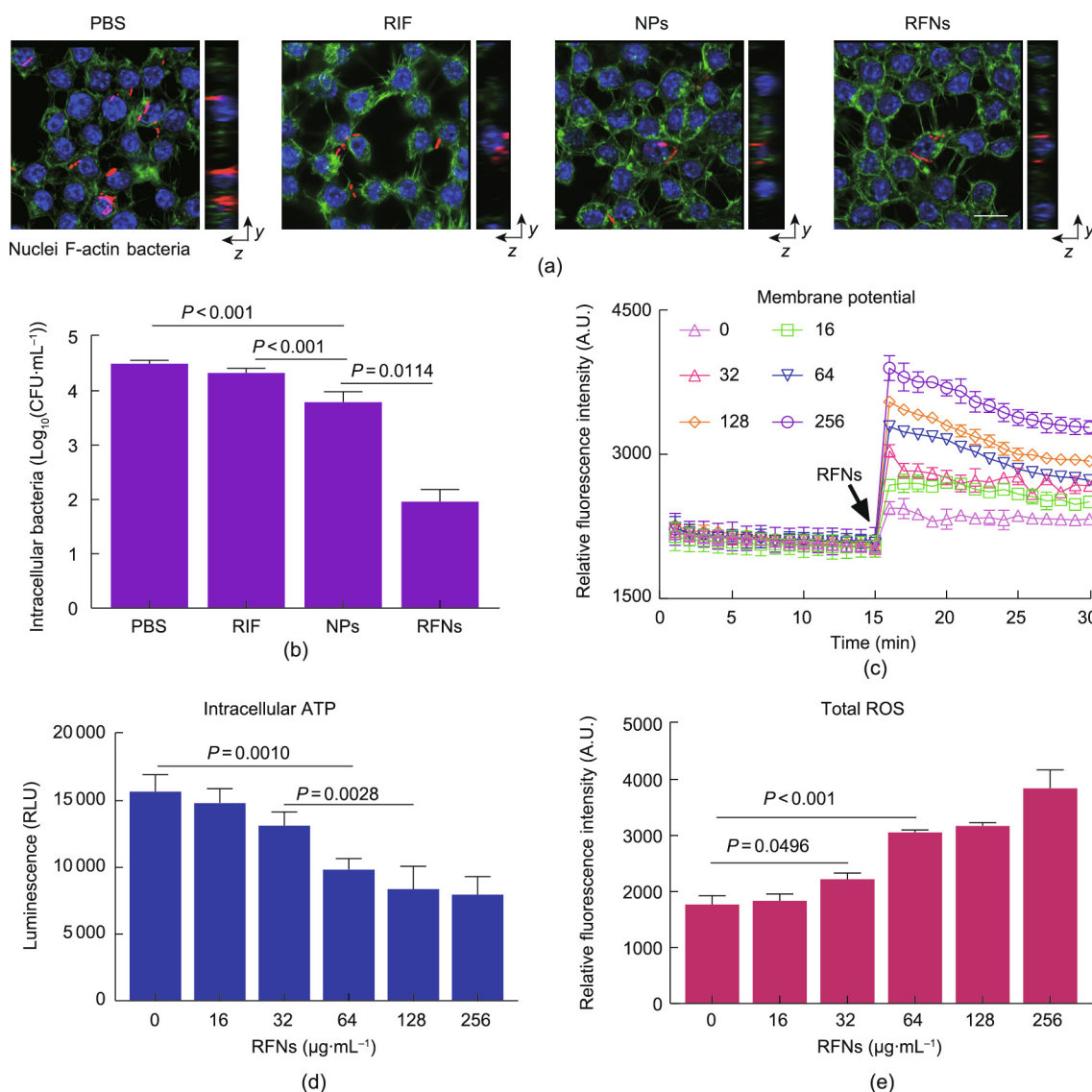

Fig. 4. RFNs effectively kill cytosolic MDR bacteria *in vitro*. (a) Confocal images of RAW 264.7 cells infected with *B. cereus* (red) in the presence of RIF, NPs, or RFNs for 4 h. Nuclei (blue) and actin (green) were stained with DAPI and Actin Green 488, respectively. Scale bar: 10 μm. (b) Quantification of cytosolic bacteria in RAW 264.7 cells after different treatments at concentrations corresponding to 10-fold MIC for 4 h. (c) Dissipated membrane potential in *B. cereus* treated with RFNs at different concentrations (0, 16, 32, 64, 128, and 256 μg·mL^{-1}) and stained with DiSC$_3$(5) (excitation/emission wavelength at 622 nm/670 nm). (d) Decreased intracellular ATP in *B. cereus* incubated with RFNs, using a luminescent ATP test. (e) Accumulation of ROS in *B. cereus* was determined by measuring the fluorescence intensity of 2′,7′-dichlorofluorescein diacetate (excitation/emission wavelength at 488 nm/525 nm) in the presence of RFNs. All data are presented as means ± SD. Statistical analysis was determined by nonparametric one-way ANOVA. RLU: relative light units.
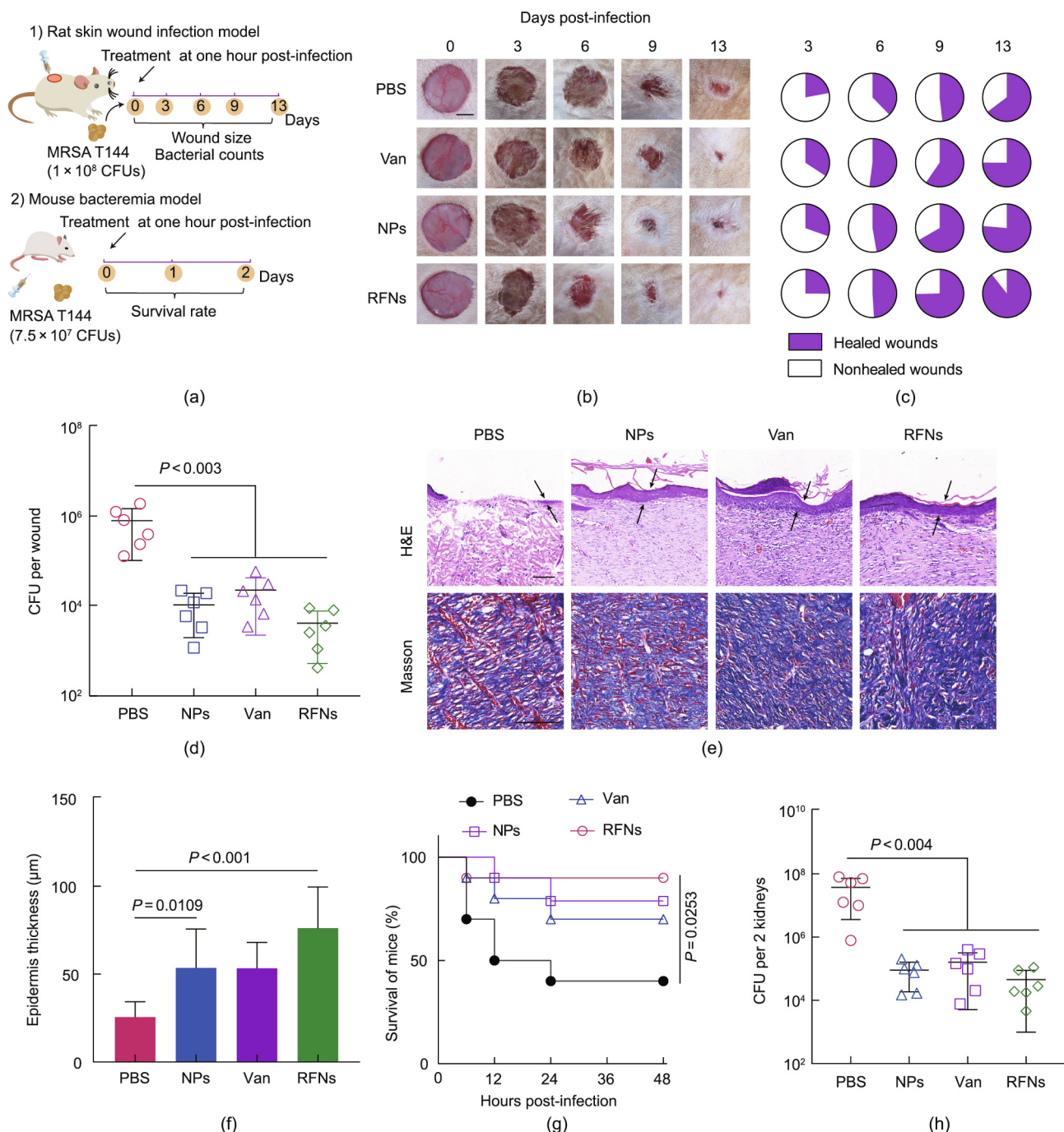
Fig. 5. Antibiotic-laden RFNs eradicate MRSA-associated infection in two animal infection models. (a) Schematic diagrams of the experimental protocol for the rat skin wound infection model and mouse bacteremia model. (b) Representative photographs of infected wounds with MRSA T144 (1×10^8 CFUs per wound) after treatments with Van (5 mg·kg^{-1}), NPs, or RFNs (equivalent to 2 mg·kg^{-1} RIF). Scale bar: 1 cm. (c) Fractions of the wounds healed were recorded after different treatments on days 3, 6, 9, and 13. (d) Bacterial loads in the rat skin wound infection model. At 13 d after infection, decreased bacterial loads were found in infected wounds treated with RFNs. (e) Representative photomicrographs of H&E and Masson staining of the wounded skin. The arrow indicates the epidermis. Scale bar: 100 μm. (f) Increased epithelial gap in the wounds treated with RFNs. Statistical analysis was performed by nonparametric one-way ANOVA. (g) Survival curves of mice in the bacteremia model after intravenous infection with MRSA T144 (7.5 × 10^7 CFUs) treated with Van (5 mg·kg^{-1}), NPs, or RFNs (equivalent to 2 mg·kg^{-1} RIF). Statistical analysis was performed by the log-rank (Mantel-Cox) test. (h) Quantification of MRSA T144 recovered from two kidneys. The bacterial loads in these kidneys were significantly decreased after treatment with RFNs for 2 d. Statistical analysis was performed by nonparametric one-way ANOVA.

to 2 mg·kg^{-1} RIF) were nearly 100% healed in 13 (Figs. 5(b) and (c)), while Van (5 mg·kg^{-1}) treatment healed only 75% of the wounds. Van has been used as the gold-standard treatment for MRSA infections for decades [32]. The antibody-rifalogue conjugate was more efficacious against MRSA infection than Van, which can be attributed to the poor efficacy of Van against intracellular bacteria [6]. RFNs promoted the accumulation of intracellular antibiotics,

thereby eliminating more MRSA and accelerating wound healing (Fig. 5(d)). These results indicate that RFNs are effective in combating MRSA infection and promoting wound healing.

To further assess the role of RFNs in wound healing, the histology of the wounds was examined using H&E and Masson's trichrome staining on day 13. RFNs significantly increased the epithelial gap thickness to promote wound re-epithelialization

Engineering 15 (2022) 57–66

(Figs. 5(e) and (f)). Furthermore, re-epithelialization and tissue remodeling were accelerated by increased collagen deposition in RFN treatment through the facilitation of extracellular matrix reorganization (Fig. 5(e)). These results were consistent with the physiological restoration and regeneration of acute wounds during the promotion of wound healing [33]. After RFN therapy, the wound-closure time was significantly shortened by three days and the body weight was significantly increased on day 13 compared with PBS treatment, which further demonstrated the better wound healing ability and efficiency of RFNs (Fig. S18 in Appendix A). Inflammatory factors were also significantly reduced by 50% after local RFN therapy compared with the model group (Fig. S19 in Appendix A), which is closely correlated with the RFNs' antibacterial efficiency. All of these results show that RFNs are biocompatible and highly effective for the treatment of acute wound infections.

The protective ability of RFNs against bacterial infection was further evaluated in a bacteremia mouse model. Mice were injected with MRSA T144 cells (7.5×10^7 CFUs) through the tail vein. One hour post-infection, mice treated with RFNs (equivalent to 2 mg·kg^{-1} RIF) showed a significantly increased survival rate (90.0%) compared with the PBS group (survival rate of 40.0%) (Fig. 5(g)). Moreover, the bacterial loads in different organs (heart, liver, spleen, lung, and kidney) decreased significantly after intravenous administration of RFNs for two days (Fig. 5(h) and Fig. S20 in Appendix A). Organ histopathology of the mice further confirmed the antibacterial activity of the RFNs. Mice that received RFN treatment had no significant pathological changes, such as atraumatic splenic hemorrhage or kidney lesions (Fig. S21 in Appendix A). These results demonstrate the potential of RFNs as an efficient antibiotic delivery platform against MDR bacterial infections.

4. Discussion

Because of the high level of concealment and antibiotic tolerance of invasive bacteria in host cells, effective elimination of such bacteria is difficult [34]. Studies have shown that subcellular structure plays an important role in the invasion and survival of bacterial pathogens in cells [35,36]. Therefore, it is critical to develop efficient carriers to deliver antibacterial drugs precisely into subcellular compartments. Nanoparticles with specific surface modifications and increased rigidity hold promise for achieving enhanced cellular uptake and precise subcellular targeting [37–39], and lipid nanoparticles are widely used as drug and gene delivery systems [40]. Tailoring the phospholipid composition of nanoparticles is an effective way to modulate their cellular internalization [41]. In this work, we designed a rigid antibiotic delivery system by loading RIF into MSNs and coating the particles with bacteria-responsive phospholipids to combat cytosolic bacterial infections. These RFNs have the characteristics of lipid nanomaterials, which are easy to adjust and modify, as well as rigidity provided by the mesoporous silica core to enhance cellular uptake by means of endocytosis. Previous studies have shown that nanoparticle rigidity is a key parameter governing cellular uptake [14]. A decrease in the cellular uptake caused by morphological changes during the endocytosis process was avoided with the increased rigidity of RFNs [15]. Modulation of the electrostatic effects of RFNs by adjusting the proportion of phospholipids on the surface allows the selective localization of payloads to their targeted subcellular compartments. The efficiency and safety of RFNs are maximized by the phospholipase-controlled drug release in lysosomes.

Our strategy successfully circumvents the treatment limitations of antibiotics against infections with cytosolic bacteria by incorporating a system that simultaneously possesses increased rigidity, subcellular targeting, and environmental responsiveness.

Therefore, we primarily conclude that the antibacterial process of RFNs should occur in a stepwise manner, as follows: ① precise recognition of the targeted bacterial pathogens; ② a rigidity-enhanced rate of endocytosis; ③ reprogrammable drug distribution; and ④ cytosolic bacterial killing.

5. Conclusions

The fabrication of safe, effective, and tunable nanoplatforms for precise cytosolic drug delivery is a serious challenge. In this study, we showed that RFNs are a potent delivery platform that combats MDR bacteria-associated infections in vitro and in vivo by actively targeting subcellular compartments and triggering the on-demand release of antibiotics. Altering the phospholipid composition of RFNs enhanced their lysosomal targeting, thereby enhancing their efficiency through increased antibiotic accumulation. Moreover, phospholipase derived from bacteria could hydrolyze the surface of the RFNs to minimize antibiotic side-effects and selective pressure. Thus, RFNs offer a promising strategy for combating cytosolic bacteria, a key issue in healthcare.

This work was supported by the Laboratory of Lingnan Modern Agriculture Project (NT2021006) and State Key Laboratory of Veterinary Biotechnology Foundation (SKLVBF202102).

Compliance with ethics guidelines

Shaoqi Qu, Xiaoyong Huang, Xiangbin Song, Yifan Wu, Xiaowei Ma, Jianzhong Shen, and Kui Zhu declare that they have no conflict of interest or financial conflicts to disclose.

Appendix A. Supplementary data

Supplementary data to this article can be found online at https://doi.org/10.1016/j.eng.2021.12.021.

References

[1] Kupferschmidt K. Resistance fighters. Science 2016;352(6287):758–61.
[2] Turner NA, Sharma-Kuinkel BK, Maskarinec SA, Eichenberger EM, Shah PP, Carugati M, et al. Methicillin-resistant Staphylococcus aureus: an overview of basic and clinical research. Nat Rev Microbiol 2019;17(4):203–18.
[3] Liu J, Gefen O, Ronin I, Bar-Meir M, Balaban NQ. Effect of tolerance on the evolution of antibiotic resistance under drug combinations. Science 2020;367(6474):200–4.
[4] Fridman O, Goldberg A, Ronin I, Shoresh N, Balaban NQ. Optimization of lag time underlies antibiotic tolerance in evolved bacterial populations. Nature 2014;513(7518):418–21.
[5] Ling LL, Schneider T, Peoples AJ, Spoering AL, Engels I, Conlon BP, et al. A new antibiotic kills pathogens without detectable resistance. Nature 2015;517(7535):455–9.
[6] Liu X, Liu F, Ding S, Shen J, Zhu K. Sublethal levels of antibiotics promote bacterial persistence in epithelial cells. Adv Sci 2020;7(18):1900840.
[7] Li Y, Liu F, Zhang J, Liu X, Xiao P, Bai H, et al. Efficient killing of multidrug-resistant internalized bacteria by AIEgens in vivo. Adv Sci 2021;8(9):2001750.
[8] Yang ZQ, Huang YL, Zhou HW, Zhang R, Zhu K. Persistent carbapenem-resistant Klebsiella pneumoniae: a Trojan horse. Lancet Infect Dis 2018;18(1):22–3.
[9] Durand GA, Raoult D, Dubourg G. Antibiotic discovery: history, methods and perspectives. Int J Antimicrob Agents 2019;53(4):371–82.
[10] Lewis K. The science of antibiotic discovery. Cell 2020;181(1):29–45.
[11] Zeng X, Liu G, Tao W, Ma Y, Zhang X, He F, et al. A drug-self-gated mesoporous antitumor nanoplatform based on pH-sensitive dynamic covalent bond. Adv Funct Mater 2017;27(11):1605985.
[12] Hood RL, Andriani RT, Ecker TE, Robertson JL, Rylander CJ. Characterizing thermal augmentation of convection-enhanced drug delivery with the fiberoptic microneedle device. Engineering 2015;1(3):344–50.
[13] Cheng W, Zeng X, Chen H, Li Z, Zeng W, Mei L, et al. Versatile polydopamine platforms: synthesis and promising applications for surface modification and advanced nanomedicine. ACS Nano 2019;13(8):8537–65.

[14] Sun J, Zhang L, Wang J, Feng Q, Liu D, Yin Q, et al. Tunable rigidity of (polymeric core)–(lipid shell) nanoparticles for regulated cellular uptake. Adv Mater 2015;27(8):1402–7.

[15] Hui Y, Yi X, Wibowo D, Yang G, Middelberg APJ, Gao H, et al. Nanoparticle elasticity regulates phagocytosis and cancer cell uptake. Sci Adv 2020;6(16): eaaz4316.

[16] Yang X, Qiu Q, Liu G, Ren H, Wang X, Lovell JF, et al. Traceless antibiotic-crosslinked micelles for rapid clearance of intracellular bacteria. J Control Release 2022;341:329–40.

[17] Lin A, Liu Y, Zhu X, Chen Xu, Liu J, Zhou Y, et al. Bacteria-responsive biomimetic selenium nanosystem for multidrug-resistant bacterial infection detection and inhibition. ACS Nano 2019;13(12):13965–84.

[18] Hu CM, Fang RH, Copp J, Luk BT, Zhang L. A biomimetic nanosponge that absorbs pore-forming toxins. Nat Nanotechnol 2013;8(5):336–40.

[19] Ye M, Zhao Yi, Wang Y, Zhao M, Yodsanit N, Xie R, et al. A dual-responsive antibiotic-loaded nanoparticle specifically binds pathogens and overcomes antimicrobial-resistant infections. Adv Mater 2021;33(9):2006772.

[20] Wu W, Yu L, Jiang Q, Huo M, Lin H, Wang L, et al. Enhanced tumor-specific disulfiram chemotherapy by *in situ* Cu^{2+} chelation-initiated nontoxicity-to-toxicity transition. J Am Chem Soc 2019;141(29):11531–9.

[21] Peyrusson F, Varet H, Nguyen TK, Legendre R, Sismeiro O, Coppée JY, et al. Intracellular *Staphylococcus aureus* persisters upon antibiotic exposure. Nat Commun 2020;11(1):2200.

[22] Xie J, Liu Y, Yang J, Liu Y, Hu F, Zhu K, et al. Gold nanoclusters for targeting methicillin-resistant *Staphylococcus aureus in vivo*. Angew Chem Int Ed Engl 2018;57(15):3958–62.

[23] Guo P, Liu D, Subramanyam K, Wang B, Yang J, Huang J, et al. Nanoparticle elasticity directs tumor uptake. Nat Commun 2018;9(1):130.

[24] Hu D, Deng Y, Jia F, Jin Q, Ji J. Surface charge switchable supramolecular nanocarriers for nitric oxide synergistic photodynamic eradication of biofilms. ACS Nano 2020;14(1):347–59.

[25] Zhu G, Mock JN, Aljuffali I, Cummings BS, Arnold RD. Secretory phospholipase A₂ responsive liposomes. J Pharm Sci 2011;100(8):3146–59.

[26] Cook AB, Decuzzi P. Harnessing endogenous stimuli for responsive materials in theranostics. ACS Nano 2021;15(2):2068–98.

[27] Iwasaki H, Shimada A, Yokoyama K, Ito E. Structure and glycosylation of lipoteichoic acids in *Bacillus* strains. J Bacteriol 1989;171(1):424–9.

[28] Ramírez-García PD, Retamal JS, Shenoy P, Imlach W, Sykes M, Truong N, et al. A pH-responsive nanoparticle targets the neurokinin 1 receptor in endosomes to prevent chronic pain. Nat Nanotechnol 2019;14(12):1150–9.

[29] Berthold-Pluta A, Pluta A, Garbowska M. The effect of selected factors on the survival of *Bacillus cereus* in the human gastrointestinal tract. Microb Pathog 2015;82:7–14.

[30] Brynildsen MP, Winkler JA, Spina CS, MacDonald IC, Collins JJ. Potentiating antibacterial activity by predictably enhancing endogenous microbial ROS production. Nat Biotechnol 2013;31(2):160–5.

[31] Qu S, Liu Y, Hu Q, Han Y, Hao Z, Shen J, et al. Programmable antibiotic delivery to combat methicillin-resistant *Staphylococcus aureus* through precision therapy. J Control Release 2020;321:710–7.

[32] Morrisette T, Alosaimy S, Abdul-Mutakabbir JC, Kebriaei R, Rybak MJ. The evolving reduction of vancomycin and daptomycin susceptibility in MRSA-salvaging the gold standards with combination therapy. Antibiotics 2020;9 (11):762–82.

[33] Xi Y, Ge J, Guo Y, Lei B, Ma PX. Biomimetic elastomeric polypeptide-based nanofibrous matrix for overcoming multidrug-resistant bacteria and enhancing full-thickness wound healing/skin regeneration. ACS Nano 2018;12(11):10772–84.

[34] Schulz F, Horn M. Intranuclear bacteria: inside the cellular control center of eukaryotes. Trends Cell Biol 2015;25(6):339–46.

[35] Choy A, Dancourt J, Mugo B, O'Connor TJ, Isberg RR, Melia TJ, et al. The Legionella effector RavZ inhibits host autophagy through irreversible Atg8 deconjugation. Science 2012;338(6110):1072–6.

[36] Garzoni C, Kelley WL. Staphylococcus aureus: new evidence for intracellular persistence. Trends Microbiol 2009;17(2):59–65.

[37] Labib M, Wang Z, Ahmed SU, Mohamadi RM, Duong B, Green B, et al. Tracking the expression of therapeutic protein targets in rare cells by antibody-mediated nanoparticle labelling and magnetic sorting. Nat Biomed Eng 2021;5 (1):41–52.

[38] Pesce D, Wu Y, Kolbe A, Weil T, Herrmann A. Enhancing cellular uptake of GFP via unfolded supercharged protein tags. Biomaterials 2013;34(17):4360–7.

[39] Kankala RK, Han YH, Na J, Lee CH, Sun Z, Wang SB, et al. Nanoarchitectured structure and surface biofunctionality of mesoporous silica nanoparticles. Adv Mater 2020;32(23):1907035.

[40] Hajj KA, Ball RL, Deluty SB, Singh SR, Strelkova D, Knapp CM, et al. Branched-tail lipid nanoparticles potently deliver mRNA *in vivo* due to enhanced ionization at endosomal pH. Small 2019;15(6):1805097.

[41] Abumanhal-Masarweh H, da Silva D, Poley M, Zinger A, Goldman E, Krinsky N, et al. Tailoring the lipid composition of nanoparticles modulates their cellular uptake and affects the viability of triple negative breast cancer cells. J Control Release 2019;307:331–41.